Nanoscale

PAPER

View Article Online
View Journal | View Issue

Cite this: *Nanoscale*, 2021, **13**, 18311

Predictions of attainable compositions of layered quaternary *i*-MAB phases and solid solution MAB phases†

Martin Dahlqvist * and Johanna Rosen*

Received 22nd April 2021,
Accepted 22nd October 2021

DOI: 10.1039/d1nr02552j

rsc.li/nanoscale

MAB phases are layered materials combining metallic and ceramic attributes. Their ternary compositions, however, have been limited to a few elemental combinations which makes controlled and tailored properties challenging. Inspired by the recent discovery of $Mo_{4/3}Y_{2/3}AlB_2$ and $Mo_{4/3}Sc_{2/3}AlB_2$ *i*-MAB phases, *i.e.*, quaternary layered MAB phases with in-plane chemical order, we perform an extensive first-principles study to explore formation of chemical order and solid-solutions upon metal alloying of M_2AB_2 phases of 1092 compositions (*M* from group 3 to 9 and *A* = Al, Ga, In, Si, Ge, Sn). This large dataset provides 39 chemically ordered (*i*-MAB) and 52 solid solution (MAB) phases that are predicted to be thermodynamically stable at typical synthesis temperatures, of which a majority have not yet been experimentally reported. The possibility for realizing both *i*-MAB and solid solution MAB phases, combined with the multiple elemental combinations previously not observed in these boride-based materials, allows for an increased potential for property tuning and potential chemical exfoliation into 2D derivatives.

Introduction

The spurred interest in layered ternary transition metal borides like M_2AlB_2 (*M* = Cr, Mn, Fe in space group *Cmmm*),[1–6] M_3AlB_4 (*M* = Cr in space group *Immm*),[3,7,8] M_4AlB_6 (*M* = Cr in space group *Cmmm*),[5,7] *M*AlB (*M* = Mo, W in space group *Cmcm*),[9–11] and M_4AlB_4 (*M* = Cr in space group *Immm*)[12] comes from the discovery of, *e.g.*, magnetocaloric properties,[4] high-temperature oxidation resistance,[13] and electrocatalytic properties.[14,15] Another potential area is to use these materials as precursors for being exfoliated into two-dimensional (2D) counterparts, MBenes, however, realization of individual single-layer sheets remains a quest.[14,16–20]

In 2015 these phases were collectively coined MAB phases by Ade and Hillebrecht due to their resemblance with layered carbide and nitride MAX phases, where *M* is an early transition metal, *A* is mostly a group 13 or 14 element (*e.g.* Al, Ga, and Si), and *X* is C and/or N.[5] MAB phases typically have an orthorhombic crystal structure, but with the recent addition of Ti_2InB_2 in space group $P\bar{6}m2$, hexagonal symmetry was introduced to the family.[21] In a follow-up theoretical work, five M_2AB_2 and two M_3AB_4, all with a hexagonal crystal structure, were predicted to be stable.[22]

The attainable chemistries in synthesized MAB phases have for a long time been limited to *A* = Al and *M* = Cr, Mo, W, Mn, and Fe, apart from the recently discovered Ti_2InB_2. A route for expanding attainable compositions of MAB phases is through alloying by adding a fourth element on *M*, *A*, or B sites. This allows for property tuning and has been realized for disordered solid-solution MAB phases $(Mo_{1-x}W_x)AlB$ and $(Mo_{1-x}Cr_x)AlB$ with *Cmcm* symmetry,[23,24] $(Fe_{1-x}M_x)_2AlB_2$ (*M* = Fe, Co) and $(Mn_{1-x}Cr_x)_2AlB_2$ with *Cmmm* symmetry.[25–28] and $(Mn_{1-x}Cr_x)_3AlB_4$ with *Immm* symmetry.[25] Potential out-of-plane ordering with alternating *M*-layers based on one *M*-element only have been investigated theoretically in the Cr_3AlB_4 crystal structure (with *Immm* symmetry) although experimental verification is awaiting.[29] Alloying on the *A*-site has been less explored with limited solubility of Si ($x \geq 0.03$) in $MoAl_{1-x}Si_xB$.[30]

Alloying has been demonstrated as an attainable path towards expanding chemistries in materials resembling the MAB phases (MAX phases) resulting in either a solid solution or a chemically ordered (*o*-MAX with two metals ordered out-of-plane and *i*-MAX with two metals ordered in-plane) distribution of the alloying elements.[31–33] In a similar way, an ordered distribution of alloying elements is possible in MAB phases other than disordered solid solutions. Recently, we considered metal alloying as a path towards expanding the attainable chemistries in orthorhombic and hexagonal M_2AlB_2 phases, and discovered two in-plane ordered MAB phases,

Materials Design, Department of Physics, Chemistry and Biology (IFM), Linköping University, SE-581 83 Linköping, Sweden. E-mail: martin.dahlqvist@liu.se, johanna.rosen@liu.se

†Electronic supplementary information (ESI) available. See DOI: 10.1039/d1nr02552j

$Mo_{4/3}Y_{2/3}AlB_2$ and $Mo_{4/3}Sc_{2/3}AlB_2$,[34] coined *i*-MAB in analogy to *i*-MAX.[35] This finding was accompanied with theoretical stability predictions of an additional 13 chemically ordered *i*-MAB phases and 16 solid solution MAB phases. This exemplifies alloying as a prospective path towards expanding the MAB phase chemistries, which combined with the various MAB structures would allow for a range of possibilities when it comes to novel elemental combinations, bond modification, and property tuning. Bond modification in a MAB phase could for example allow for potential conversion into its 2D derivative, in the same way as conversion of *i*-MAX to *i*-MXene.[36]

In this work we use a systematic theoretical approach which includes high-throughput stability predictions to demonstrate an expansion of the possible chemistries for quaternary M_2AB_2 phases, $(M'_{1-x}M''_x)_2AB_2$, beyond A = Al, by exploiting metal alloying. We consider both chemically ordered (*i*-MAB) and a solid solution distribution of M' and M'', the latter by considering both the *Cmmm* and $P\bar{6}m2$ space group symmetries. We considered a 2 : 1 ratio of M' and M'' motivated by the in-depth investigation in ref. 34 where further details can be found. In short, a 2 : 1 ratio allows in-plane chemical ordering, as confirmed in experiments. A ratio diverging significantly from 2 : 1, such as 3 : 1 or 1 : 1, will likely give a solid solution, if such composition is stable. In a previous report, the related in-plane ordered *i*-MAX phase $(Mo_{2/3}Sc_{1/3})_2AlC$ were investigated and it was demonstrated that small compositional deviations from the ideal 2 : 1 ratio is possible while still maintaining the *i*-MAX structure, however, diverging composition is detrimental for MXene formation.[37]

Guided by thermodynamic stability calculations, we confirm the stability for experimentally known i-MAB and solid solution phases. More importantly, beyond A = Al we also predict an additional 24 stable *i*-MAB phases and 36 stable solid solutions yet to be experimentally confirmed. We investigate the impact from choice of element (M', M'', and A) and the effect of size and electronegativity of M', M'' and A for the formation of chemically ordered *i*-MAB or solid solution MAB phases. We also propose guidelines for which elemental combinations to use in search for novel i-MAB and solid solution MAB phases. This study reveals that alloying is viable path towards novel elemental combinations to allow for potentially tuneable and advantageous properties.

Method

All first-principles calculations are performed by means of density functional theory (DFT) using the Vienna *ab initio* simulation package (VASP) version 5.4.1.[38–40] The projector augmented wave method is used with the generalized gradient approximation (GGA) as parameterized by Perdew–Burke–Ernzerhof (PBE).[41–43] In systems with Cr, Mn, Fe, and Co, we used the spin-polarized GGA version and energy is taken for the lowest ferromagnetic and antiferromagnetic configurations sampled within the unit cell. Further details are given in Fig. S1 and S2.† For structural relaxation, the Brillouin zone was integrated by Monkhorst–Pack special *k*-point sampling, with a density of 0.05 $Å^{-1}$ with a plane-wave energy cut-off of 400 eV.[44] The convergence of formation enthalpy with respect to the *k*-point density and plane-wave energy cut-off is shown in Fig. S3.† The convergence criterion for self-consistency is reached when satisfying an energy convergence of 10^{-6} eV per atom and force convergence of 10^{-2} eV $Å^{-1}$. Density of states (DOS) and crystal orbital Hamilton population (COHP) were retrieved using the LOBSTER code[45–48] where the calculated band-structure energy is reconstructed into orbital interactions. Positive COHP values indicate an antibonding interaction, and negative COHP values indicate a bonding interaction. Details about calculating elastic moduli are provided in ESI.†

The composition in focus is M_2AB_2 which in its ternary form have been reported in an orthorhombic *Cmmm* and hexagonal $P\bar{6}m2$ structure, where M is a transition metal and A an A-group element, see Table S1† for reported ternary M_2AB_2 phases. In this work we have considered M from group 3 to 9; Sc, Y, Ti, Zr, Hf, V, Nb, Ta, Cr, Mo, W, Mn, Fe, Co, and Ni, along with A elements; Al, Ga, In, Si, Ge, and Sn. Solid solution or chemical disorder of M' and M'' are modelled on the M sublattice for the two known M_2AB_2 crystal structures, *i.e.*, with *Cmmm* and $P\bar{6}m2$ space group symmetries, using the special quasi-random structure (SQS) method.[49] Convergency tests show that supercells with 120 atoms or more give a qualitatively accurate representation and a quantitative convergency in terms of calculated formation enthalpies, equilibrium volumes, and lattice parameters.

We assess the thermodynamic stability of a phase by comparing its energy relative to competing phases in the ternary or quaternary system of interest. This will give information whether the phase is energetically favoured or prefer decomposition into other competing phases. The most competing set of competing phases, denoted equilibrium simplex, is identified using a linear optimization procedure[50,51] which have been proven successful to confirm already experimentally materials as well as predicting the existence of new ones.[51–56] The stability of a phase is quantified in terms of the formation enthalpy ΔH_{cp} by comparing its energy to the energy of the equilibrium simplex according to

$$\Delta H_{cp} = E[(M'_{1-x}M''_x)_2AB_2] - E[\text{equilibrium simplex}]. \quad (1)$$

A phase is concluded stable when $\Delta H_{cp} < 0$. Here $E[(M'_{1-x}M''_x)_2AB_2]$ represent the chemical order of lowest energy being chemically ordered $M'_{4/3}M''_{2/3}AB_2$ or solid solution $(M'_{1-x}M''_2)_2AB_2$. However, when $T \neq 0$ K, the contribution from configurational entropy for a disordered distribution of M′ and M″ on the M sublattice in $(M'_{1-x}M''_2)_2AB_2$ will decrease the Gibbs free energy, $\Delta G_{cp}^{solidsolution}$, as approximated by

$$\Delta G_{cp}^{\text{solid solution}}[T] = \Delta H_{cp}^{\text{solid solution}} - T\Delta S. \quad (2)$$

The entropic contribution ΔS, assuming an ideal solution of M' and M'' on the M-sites, is given by

$$\Delta S = -2k_B[y\ln(y) + (1-y)\ln(1-y)], \quad (3)$$

where k_B is the Boltzmann constant and y is the concentration of M'' on the M-sublattice. Additional temperature effects, such as lattice vibrations, were not considered, as such contributions, significant or not for individual phases, tend to cancel out in the calculated stability.[57]

Visualization of atomic structures was done with the VESTA code.[58]

Results and discussion

Considered models for quaternary MAB phases

In a recent work, we investigated the thermodynamic stability upon metal alloying in M_2AlB_2 phases, and predicted 15 chemically ordered phases as well as 16 solid solutions to be stable. The study included experimental verification of chemically in-plane ordered $Mo_{4/3}Y_{2/3}AlB_2$ and $Mo_{4/3}Sc_{2/3}AlB_2$ *i*-MAB phases.[34] Here we expand the possible compositions by also including A = Ga, In, Si, Ge, and Sn. We have considered an M' and M'' ratio of 2 : 1 based on the stoichiometry of the quaternary *i*-MAB phases.[34] Moreover, this ratio also allows for a good description of possible solid solutions upon alloying in a general quaternary $(M'_{1-x}M''_2)_2AB_2$ phase as exemplified by the reported synthesis of $(Mn_{1-x}Cr_x)_2AlB_2$ with a *Cmmm* space group symmetry.[25] We have considered three different distributions of M' and M'', illustrated in Fig. 1, motivated by to date reported quaternary $(M'_{1-x}M''_2)_2AB_2$ structures and the detailed search for possible chemical ordering conducted in ref. 34; (i) solid solution in the orthorhombic M_2AB_2 structure with *Cmmm* space group symmetry, (ii) solid solution in the hexagonal M_2AB_2 structure with $P\bar{6}m2$ space group symmetry, and (iii) in-plane chemical order in *i*-MAB with four different space group symmetries ($P\bar{6}2m$, $P\bar{6}2c$, $R\bar{3}m$, $C2$). The $R\bar{3}m$ structure is shown in Fig. 1c and it is also the structure assigned for the synthesized $Mo_{4/3}Y_{2/3}AlB_2$ and $Mo_{4/3}Sc_{2/3}AlB_2$ *i*-MAB phases in ref. 34. Note that in the *i*-MAB phase, M'' is extended toward the A-layer, in turn displaying an ideal Kagomé lattice while the boron layers are hexagonal. For further details, see ref. 34.

Stability of quaternary MAB phases – chemical order *vs.* solid solution

Fig. 2a–f show the trends in thermodynamic stability for 1092 unique chemical compositions. Note that the results for A = Al have previously been presented in ref. 34. For each A element (A = Al, Ga, In, Si, Ge, Sn), a heatmap is shown where M' and M'' are assembled according to the periodic group of the M elements. The background color represents the calculated thermodynamic stability for chemical order of lowest energy, with a blue region representing stable phases ($\Delta H_{i\text{-MAB}}$ or $\Delta G_{\text{solid solution}} < 0$). $\Delta H_{i\text{-MAB}}$ is evaluated at 0 K while $\Delta G_{\text{solid solution}}$ is evaluated at 2000 K by considering the contribution from configurational entropy to the Gibb's free energy, using eqn (3), for solid solution $(M'_{0.67}M''_{0.33})_2AB_2$. This choice is motivated by a typical synthesis temperature of 1000 to 1800 °C (1273 to 2173 K) for M_2AB_2 and $(Mn_{1-x}M''_{0.2})_2AlB_2$ (M'' = Cr, Fe).[5,17,25,26,59–61] We use a symbol representation to denote the structure of lowest energy at a temperature of 2000 K; solid solution *Cmmm* (open square), solid solution $P\bar{6}m2$ (open hexagon), and *i*-MAB phases with $P\bar{6}2m$ (filled right triangle), $P\bar{6}2c$ (filled left triangle), $R\bar{3}m$ (filled up triangle) and $C2$ (filled down triangle) symmetries. In addition, experimentally known quaternary phases are marked by green squares for solid solution *Cmmm* MAB phases[25,26,59] and orange squares for ordered *i*-MAB phases.[34] A complete list of synthesized phases can be found in Tables S2 and S3.† Results evaluated at 0 K, *i.e.*, without contribution from configurational entropy to the solid solution phases, is shown in Fig. S4.† Here it should be noted that experimentally known solid solution $(M'_{1-x}M''_x)_2AlB_2$ *Cmmm* phases are predicted to be not stable at 0 K (Fig. S4†), and stable when evaluated at 2000 K (Fig. 2). This emphasizes the importance of including configurational entropy for disordered solid solution phases when evaluating the stability.

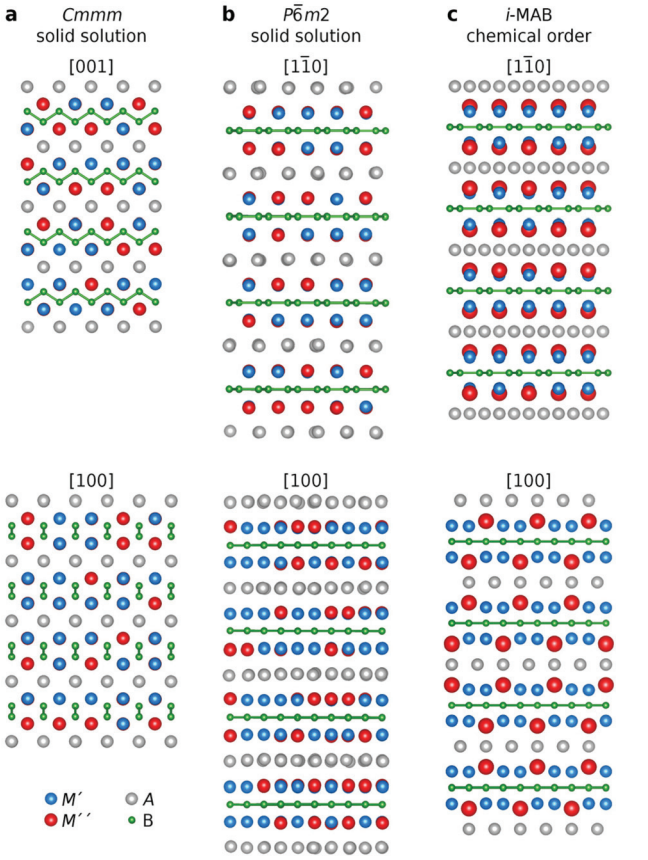

Fig. 1 Schematic illustration of various elemental distributions in quaternary 212 MAB phases upon metal alloying of M' and M''. (a) solid solution with *Cmmm* space group symmetry, (b) solid solution with $P\bar{6}m2$ space group symmetry, and (c) chemically ordered *i*-MAB with $R\bar{3}m$ space group symmetry. M', M'', A, and B elements are represented by blue, red, grey, and green atoms, respectively.

All four experimentally reported solid solution $(M'_{0.67}M''_{0.33})_2AlB_2$[25,26,59] are predicted to be stable, as well as the recently discovered $Mo_{4/3}Sc_{2/3}AlB_2$ and $Mo_{4/3}Sc_{2/3}AlB_2$

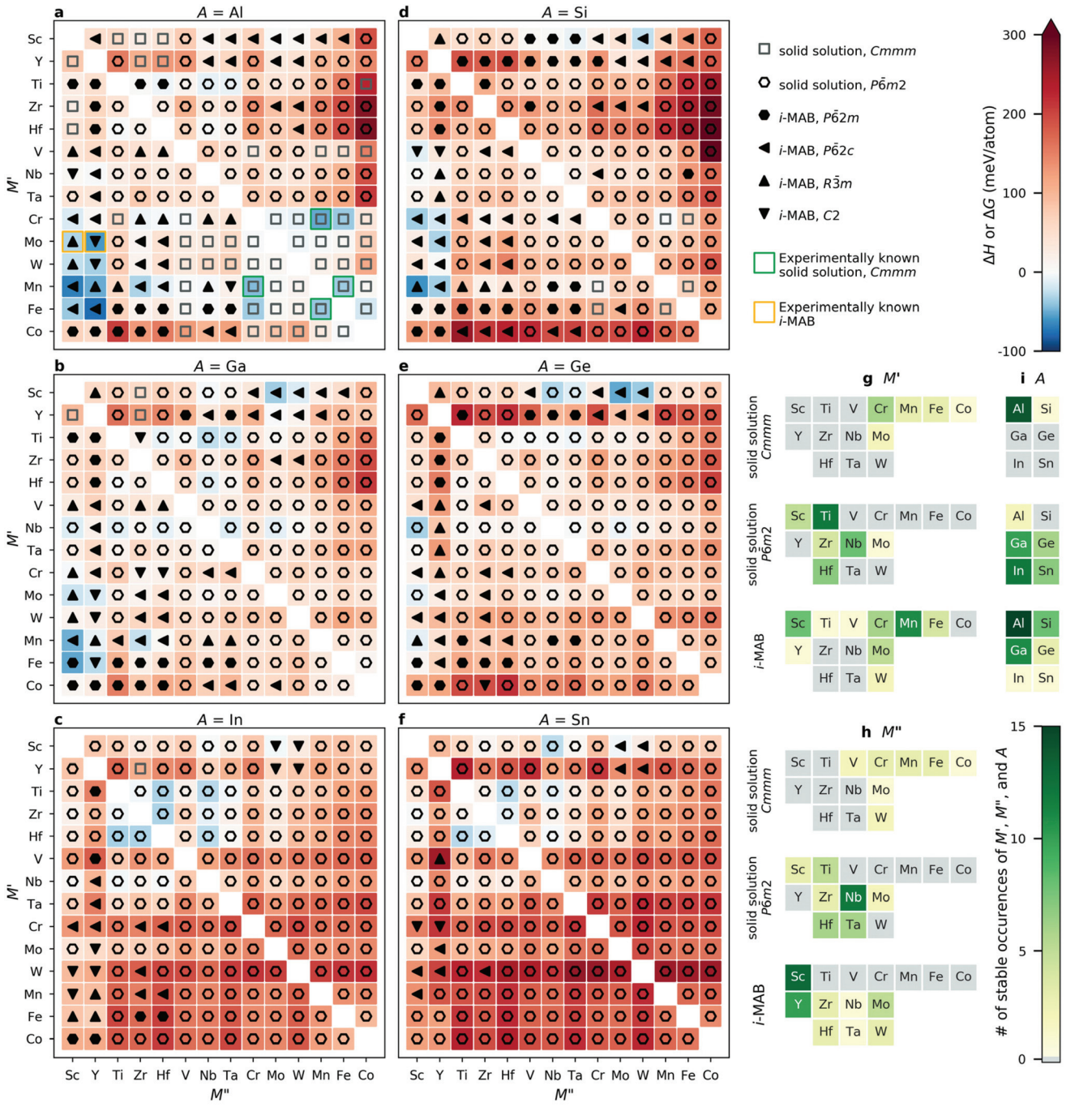

Fig. 2 (a–f) Calculated formation enthalpy ΔH (order) or and Gibbs free energy of formation (solid solution) evaluated at 2000 K for A = Al, Ga, In, Si, Ge, and Sn. Number of atomic elements in stable *i*-MAB and solid solution MAB phases for (g) M', (h) M'', and (i) A.

i-MAB phases.[34] Fig. 2g–i shows statistics for stable occurrences of M', M'', and A elements for all considered chemical configurations. In total, 39 *i*-MAB phases are predicted stable, *i.e.*, with $\Delta H_{cp} < 0$, along with 52 stable solid solutions, *i.e.*, with $\Delta G_{cp}^{solidsolution} < 0$ and $\Delta G_{cp}^{solidsolution} < \Delta H_{cp}$, out of which 15 have a *Cmmm* symmetry and 37 a $P\bar{6}m2$ symmetry.

Results for A = Al, which have been published elsewhere,[34] reveal 15 thermodynamically (Fig. 2a) and dynamically (Fig. S5–S19†) stable *i*-MAB phases with in-plane chemical ordering. Out of these, eight *i*-MAB phases have a calculated $\Delta H_{cp} < -25$ meV per atom, *i.e.* are herein judged to be significantly below zero, including $M'_{4/3}M''_{2/3}AlB_2$ (M'' = Mo, Mn, Fe and M'' = Sc, Y), $W_{4/3}Y_{2/3}AlB_2$ and $Mn_{4/3}Zr_{2/3}AlB_2$. The 16 solid solution Al-based phases predicted stable at 2000 K are dominated by the *Cmmm* symmetry, 14 compositions, combining metals mainly from group 6 to 9.

For the 11 *i*-MAB phases predicted thermodynamically stable (Fig. 2b) for A = Ga, nine is concluded to also be dynamically stable (Fig. S20–S30†). Out of these, three are identified with $\Delta H_{cp} < -25$ meV, including $M'_{4/3}Sc_{2/3}GaB_2$ (M' = Mn, Fe) and $Fe_{/3}Y_{2/3}GaB_2$. These phases are accompanied by 10 stable solid solutions with $P\bar{6}m2$ symmetry, exemplified by $(Ti_{0.67}Nb_{0.33})_2GaB_2$ with $\Delta G_{cp}^{solidsolution} = -24$ meV per atom.

For A = In (Fig. 2c), only one *i*-MAB phase, $Sc_{4/3}Mo_{2/3}InB_2$, is found to be stable, but just barely so, with $\Delta H_{cp} < -3$ meV per atom. Its dynamical stability is shown in Fig. S31.† More interesting are the 12 solid solutions with $P\bar{6}m2$ symmetry predicted stable, out of which six have $\Delta G_{cp}^{solidsolution} < -25$ meV per atom, including $(Ti_{0.67}M''_{0.33})_2InB_2$, $(Zr_{0.67}Hf_{0.33})_2InB_2$ (M'' = Hf, Nb), and $(Hf_{0.67}M''_{0.33})_2InB_2$ (M'' = Ti, Zr, Nb).

When A is from group 14, similar results are found. For A = Si, eight *i*-MAB phases are predicted to be thermodynamically stable (Fig. 2d), out of which four fulfil $\Delta H_{cp} < -25$ meV per atom, including $M'_{4/3}Sc_{2/3}AlB_2$ (M' = Cr, Mn) and $M'_{4/3}Y_{2/3}AlB_2$ (M' = Mo, Mn). Dynamical stability of these are demonstrated in Fig. S32–S39.† Only one solid solution is found stable, $(Cr_{0.67}Mn_{0.33})_2SiB_2$, with *Cmmm* symmetry. For A = Ge and Sn, four *i*-MAB phases and 13 solid solutions with $P\bar{6}m2$ symmetry are predicted stable (Fig. 2e and f). Out of these, two *i*-MAB phases are found with $\Delta H_{cp} < -25$ meV per atom, $Sc_{4/3}Mo_{2/3}GeB_2$ and $Sc_{4/3}W_{2/3}GeB_2$. Five solid solutions have $\Delta G_{cp}^{solidsolution} < -25$ meV per atom, including $(Sc_{0.67}Nb_{0.33})_2AB_2$ (A = Ge, Sn), $(Nb_{0.67}Sc_{0.33})_2GeB_2$, $(Ti_{0.67}Hf_{0.33})_2SnB_2$, and $(Hf_{0.67}Ti_{0.33})_2SnB_2$. All four thermodynamically stable *i*-MAB phases are dynamically stable (Fig. S40–S43†).

In summary, the 39 *i*-MAB phases predicted thermodynamically stable, *i.e.* with $\Delta H_{cp} < 0$, are mainly found for A = Al, Ga, and Si combined with M' = Sc, Cr, Mn, Mo and M'' = Sc and Y. Out of these, 36 *i*-MAB phases are also concluded as dynamically stable as seen by the calculated phonon dispersion (Fig. S5–S43†). The three dynamically unstable *i*-MAB phases have M' = Sc in common (Fig. S20–S21 and S33†). Stable solid solutions with $P\bar{6}m2$ symmetry are mainly found for A = Ga, In, Ge, Sn combined with M' and M'' from group 4 and 5. The 15 stable solid solution MAB phases with *Cmmm* symmetry are found for the traditional transition metals from group 6 to 9 and primarily for A = Al. These results illustrate that quaternary MAB phases, in the form of *i*-MAB or as solid solution, is a most prospective path towards expanding the attainable chemistries and structures which, in turn, allow for tuning potential. This highlights the value of computational materials discovery for accelerating exploratory synthesis in new chemical spaces. A complete list of stable *i*-MAB and solid solution phases are given in Table S4.†

Crystal symmetry and chemical order/disorder

An intuitive picture whether chemical order or solid solution is preferred for quaternary MAB phases is shown in Fig. 3 for the

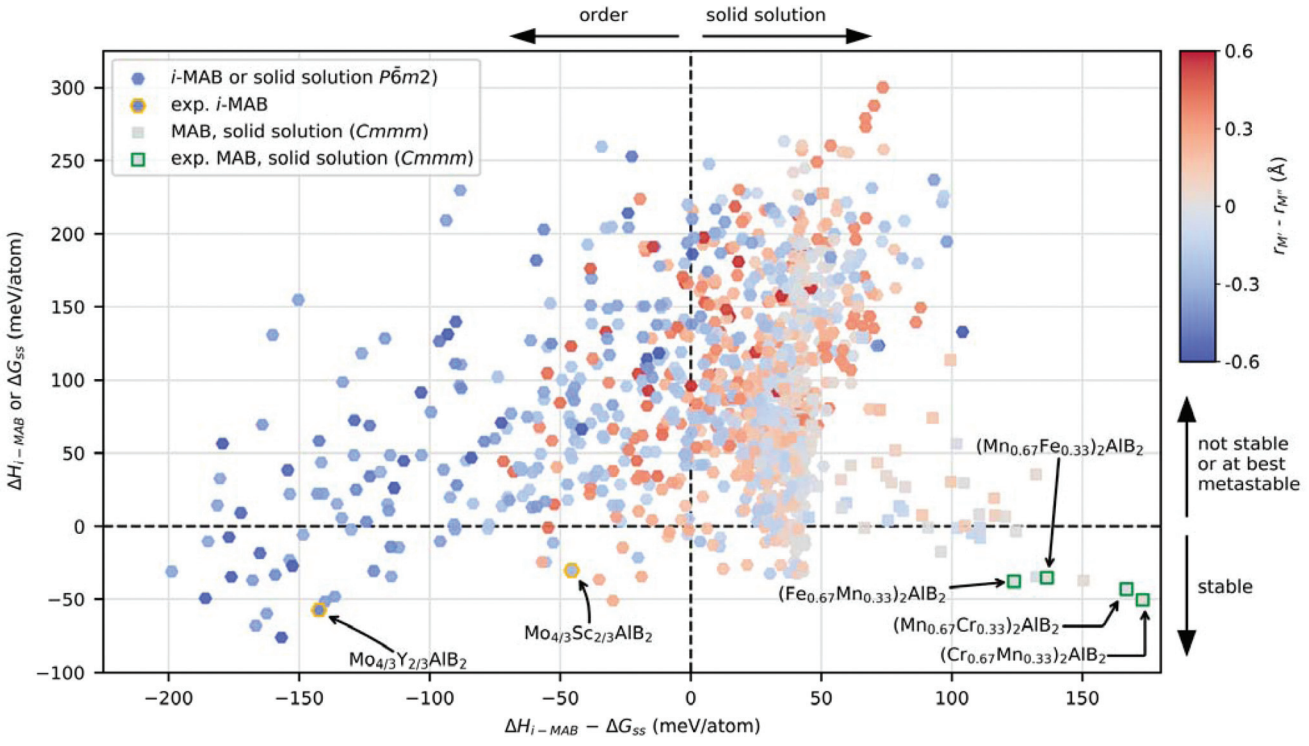

Fig. 3 Calculated formation enthalpy (*i*-MAB) or Gibbs free energy of formation at 2000 K (solid solution MAB phase) of $M'_{4/3}M''_{2/3}AB_2$ as function of energy difference between *i*-MAB and solid solution MAB for all A. The symbol represents the symmetry of lowest energy and colouring represents the atomic size difference between M' and M''. Experimentally known *i*-MAB phases are indicated by orange hexagons and solid solution MAB phases with *Cmmm* symmetry by green squares.

1092 compositions considered, where the calculated stability, represented by the lowest value of $\Delta H_{i\text{-MAB}}$ or $\Delta G_{\text{solid solution}}$ is shown as function of the energy difference between chemically ordered *i*-MAB and solid solution MAB (lowest energy of *Cmmm* or $P\bar{6}m2$), $\Delta H_{i\text{-MAB}} - \Delta G_{\text{solid solution}}$. The coloring represents the atomic size difference between M' and M'' (see Table S7† in for values used) while the symbol used represent the structure of lowest energy at 2000 K; hexagon for hexagonal *i*-MAB or solid solution, and square for orthorhombic solid solution structures. All reported synthesized *i*-MAB phases are marked by orange hexagons and solid solution MAB phases with *Cmmm* symmetry by green squares.

Thermodynamically stable *i*-MAB phases encompass 39 unique compositions which are found in the lower left quadrant of Fig. 3, among which a majority fulfill the atomic size criteria $r_{M''} > r_{M'}$ as indicated by the blue color. This includes the two synthesized *i*-MAB phases, both comprised of metal atoms with an atomic size difference, $r_{M''} > r_{M'}$, of at least 0.2 Å. Stable *i*-MAB phases are mainly represented by M' = Sc, Cr, Mn, Mo and M'' = Sc and Y, and A = Al, Ga, Si (see Fig. 2g–i). This results thus illustrates that there are many prospective *i*-MAB phases remaining to be experimentally discovered. A complete list of chemistries for stable *i*-MAB phases is found in Table S4.† Not stable, or at best metastable, *i*-MAB phases are found in the upper left quadrant of Fig. 3.

All of the reported synthesized MAB phases with solid solution of M' and M'' (Table S2†) are found stable and found in the lower right quadrant of Fig. 3. Here the atomic size difference of M' and M'' is small and typically in the range -0.2 Å < $r_{M'} - r_{M''} < 0.2$ Å. There are more than 48 hypothetical solid solution MAB phases fulfilling this criterion, a complete list thereof is found in Tables S5 and S6,† which demonstrate that there are a vast number of phases remaining to be experimentally verified. The upper right quadrant represents not stable, or at best metastable, solid solution MAB phases.

Hexagonal symmetry – impact from atom size and electronegativity

To identify the attributes governing the preference for chemical order in the *i*-MAB structure or solid solution disorder in the $P\bar{6}m2$ structure (both with hexagonal symmetry), we look at the size and electronegativity of M' and M''. Fig. 4a shows the energy difference ΔE of *i*-MAB compared to solid solution $P\bar{6}m2$ evaluated at 2000 K as function of the size difference between M' and M'', Δr_M, where $\Delta E < 0$ indicates favored *i*-MAB. Overall, ΔE is found to be correlated with the size difference, with a solid solution favored for similar size of M' and M'' while a larger difference favors *i*-MAB. This is most pronounced when M'' is larger than M', *i.e.*, $\Delta r_M < 0$. The experimentally known *i*-MAB phases are found in the region $\Delta r_M < -0.2$ Å. For all six A elements, the *i*-MAB is in general energetically favored when M' is smaller than M'' as shown in Fig. 2b. Solid solution is typically favored when $r_{M'} \approx r_{M''}$ or more specifically within a -0.2 Å < $r_{M'} - r_{M''} < 0.2$ Å range.

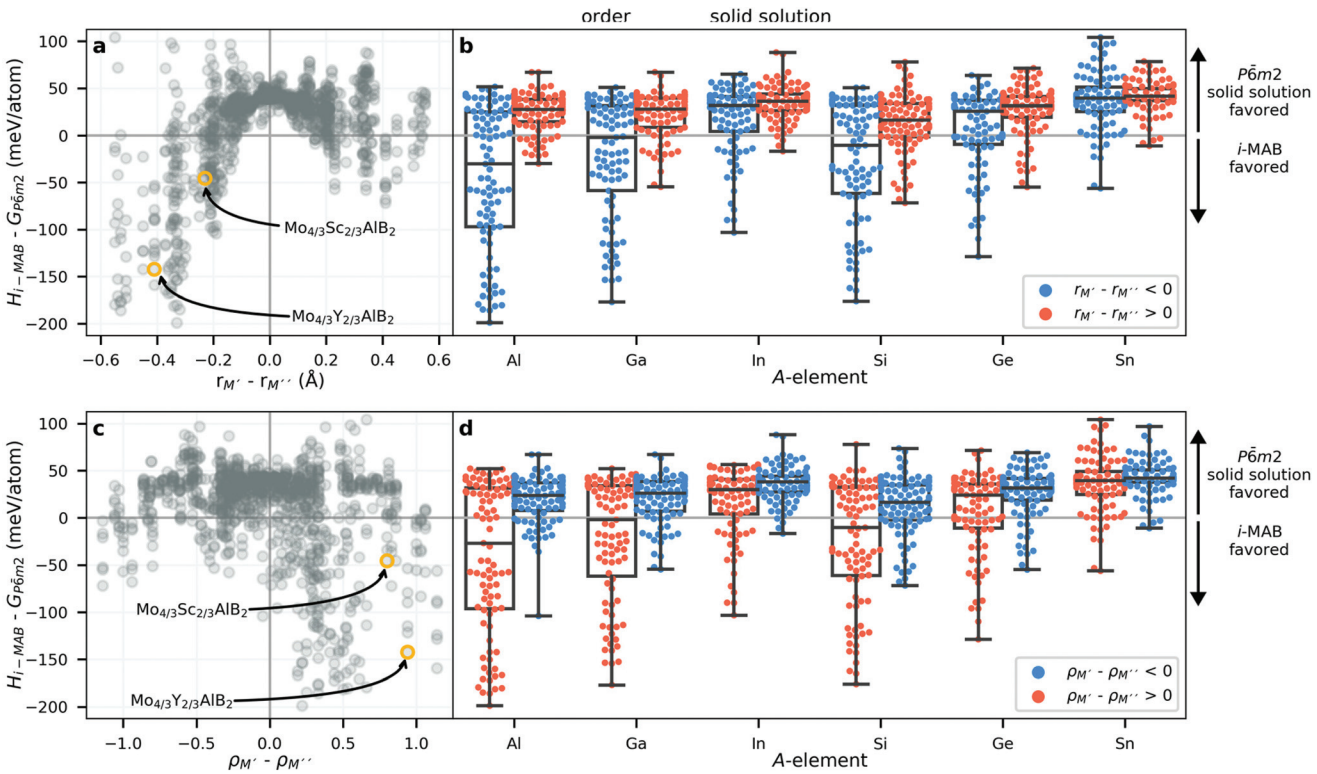

Fig. 4 Energy difference ΔE between *i*-MAB and solid solution $P\bar{6}m2$ as function of (a) size difference of M'' and M' and (c) electronegativity difference of M'' and M'. Box- and swarmplots for ΔE categorized by difference in (b) size and (d) electronegativity of M'' and M' where negative and positive values are shown in blue and red, respectively.

Next, in Fig. 4c we look at ΔE of *i*-MAB and solid solution as function of the electronegativity difference between M' and M'', $\Delta\rho_M$. Again, the region with $\Delta E < 0$ indicates favored *i*-MAB and is mostly found in the region when $\Delta\rho_M > 0$. There is no apparent correlation between ΔE and $\Delta\rho_M$, as compared to ΔE and Δr_M in Fig. 4a, with data being more scattered. However, the majority of energetically favored *i*-MAB are identified for M'' being more electronegative than M', including the recently discovered $Mo_{4/3}Sc_{2/3}AlB_2$ and $Mo_{4/3}Sc_{2/3}AlB_2$ *i*-MAB phases.[34]

Impact from choice of A, as shown in Fig. 4b and d, indicate a larger tendency for favouring *i*-MAB for A = Al, Ga, and Si, while both A = In and Sn favour formation of solid solutions. Note that both In and Sn have a larger atomic size than Al, Ga, and Si (Table S7†). This result resembles the impact from size of A as demonstrated for *i*-MAX phases.[32]

Solid solution MAB phases – impact from size and electronegativity

Next, we consider the solid solution MAB phases by comparing the orthorhombic *Cmmm* and hexagonal $P\bar{6}m2$ symmetries. Again, we choose to look at the size and electronegativity differences of M' and M'' and possible impact from choice of A element. Fig. 5a shows the energy difference ΔE of solid solutions *Cmmm* and $P\bar{6}m2$ as function of the size difference between M' and M'', Δr_M, where $\Delta E < 0$ indicates favored *Cmmm*. Here we find that *Cmmm* in general and the synthesized phases in particular are all found within -0.2 Å $< r_{M'} - r_{M''} < 0.2$ Å. Hexagonal $P\bar{6}m2$ is almost always favored when $r_{M'} - r_{M''} < -0.2$ Å or $r_{M'} - r_{M''} > 0.2$ Å but is also found within -0.2 Å $< r_{M'} - r_{M''} < 0.2$ Å. Impact for various A in Fig. 5b shows that A = Al is the element to go for if *Cmmm* symmetry is wanted, while $P\bar{6}m2$ is favored for the other A elements. It should be noted that results in Fig. 5 do not give any information regarding the stability of the material. This can be found in Fig. 2 and explicitly in Tables S4E–S6.†

In Fig. 5c we look at ΔE as function of the electronegativity difference between M' and M'', $\Delta\rho_M$. Again, the region with $\Delta E < 0$ indicates favored *Cmmm* while $\Delta E > 0$ indicates favor for $P\bar{6}m2$. Here no clear region of $\Delta\rho_M$ is identified. Neither can any clear correlation be found for various A, as shown in Fig. 5d.

Summarizing key results governing the formation of chemical ordering in *i*-MAB or solid solution, we find that for all systems, *i*-MAB is statistically the preferred structure when the size of M' is larger than M'' combined with M'' being more electronegative than M'. Comparing the difference in size (Fig. 3, 4a and b) and electronegativity (Fig. 4c and d) indicates that the former has a larger impact than the latter. The Hume-Rothery rules states that if there is a large enough difference in size and electronegativity between two atomic species, chemical order is preferred, whereas for minute differences solid

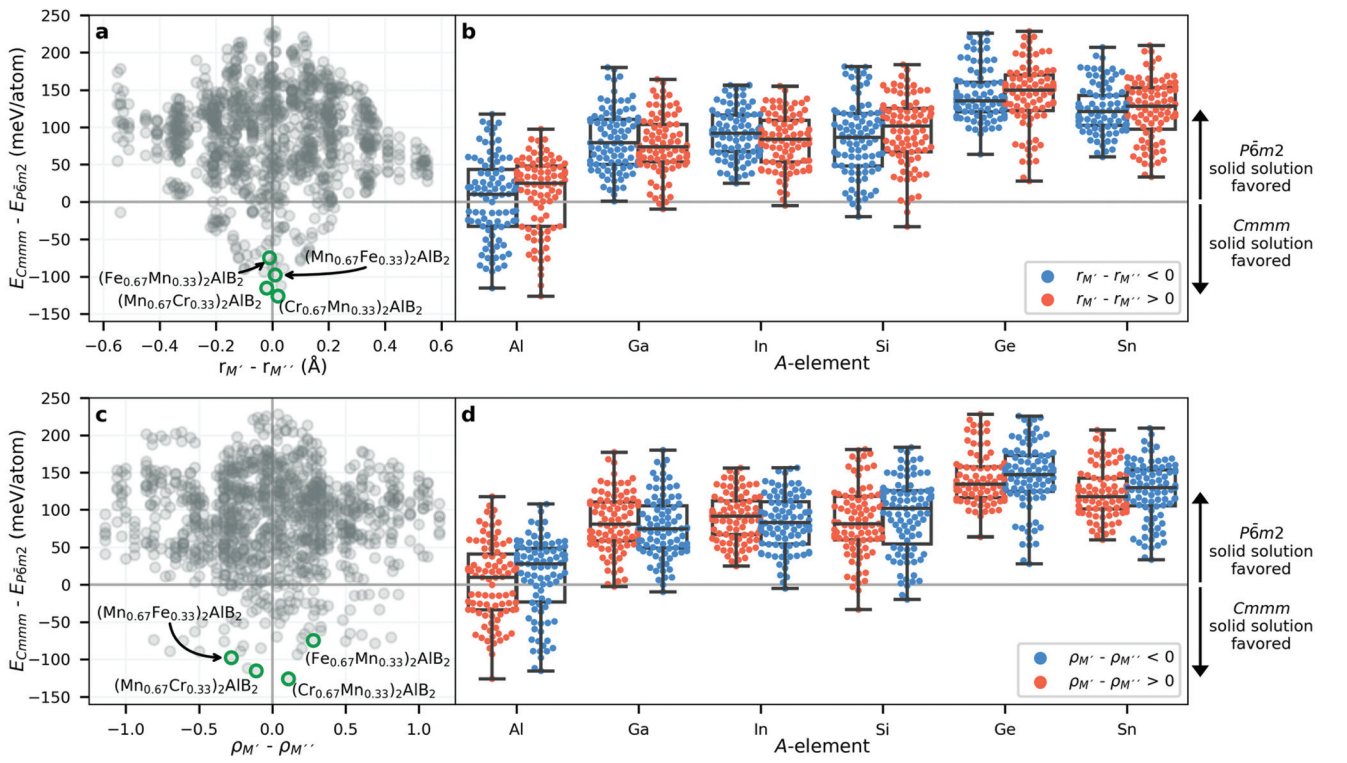

Fig. 5 Energy difference ΔE between solid solution MAB phases with *Cmmm* and $P\bar{6}m2$ symmetry as function of (a) size difference of M'' and M' and (c) electronegativity difference of M'' and M'. Box- and swarmplots for ΔE categorized by difference in (b) size and (d) electronegativity of M'' and M' where negative and positive values are shown in blue and red, respectively. Experimentally reported solid solution MAB phases with *Cmmm* symmetry are marked in panel (a) and (c).

solution is favored.[62] Metal alloying in 212 MAB phases thus partly fulfills the Hume-Rothery rules as demonstrated by preference for *i*-MAB only when M'' is larger than M', as indicated by the blue colour in Fig. 3 and the left part of Fig. 4a. When M' and M'' is of similar size, solid solution is the energetically favoured order. It should be noted that the original Hume-Rothery rules are restricted to binary compounds. For higher order systems, specific rules need to be established for each system alone since they are dependent on the crystal structure, its sublattices and elements involved, as demonstrated herein and elsewhere.[32,63,64]

Properties of selected i-MAB phases

We choose to focus on the impact that different *A*-elements may have on the electronic and mechanical properties for selected *i*-MAB phases, namely $Mo_{4/3}Y_{2/3}AB_2$ with *A* = Al, Ga, Si. These materials were chosen motivated by the $M' + M''$ combination being predicted stable for three different *A*-elements (Fig. 2) and that $Mo_{4/3}Y_{2/3}AlB_2$ have been synthesized. Note that the space group symmetries of lowest energy – $P\bar{6}2c$, $R\bar{3}m$, $C2$ – are close to degenerate in energy. Hence, for simplicity we here only include the $R\bar{3}m$ structure for a comparison of the properties. Data for $P\bar{6}2c$ and $C2$ can be found in the ESI.†

The calculated electronic structure in terms of density of states (DOS) for selected *i*-MAB phases, with *A* = Al, Ga, Si in space group $R\bar{3}m$, are plotted in the upper panels of Fig. 6. The change of *A*-element does not significantly affect the overall electronic structure, with the most notable change arising from a shift in the Fermi level for *A* = Si as compared to *A* = Al and Ga. This can be related to Si having one additional valence electron. For *A* = Al and Ga there are no significant qualitative difference which can be explained by the equivalent valency of Al and Ga. DOS for the other symmetries is shown in Fig. S44–S46 in ESI.† Due to the similarities in structure and layering, they are qualitatively equivalent with the results obtained for $R\bar{3}m$.

All *i*-MAB phases show an evident metallic character with a finite number of states at and around the Fermi level. This is also reflected in the electronic band-structures (Fig. S49–S57†) where a multitude of bands are crossing the Fermi level, along with a lack of significant anisotropy, which further confirms the metallicity of these materials.

The corresponding COHP analysis is plotted in the bottom panels of Fig. 6 for selected key interactions. The results show that all three *i*-MAB phases are found to be close to optimized from a bonding perspective. A slight but notable change in the distribution of bonding and antibonding states can be observed when going from Al and Ga to Si. Most states at and in the vicinity of the Fermi level can be attributed to non-bonding Mo-*d*. Additional bonding characteristics for the other symmetries is shown in Fig. S47–S48.†

The similarities and differences between the phases can also be quantified by integrating the occupied states of the COHP curve (ICOHP) and then comparing the contribution (in percentage) of the pairwise interactions with respect to the net (total) integrated bonding within each *i*-MAB phase. This is seen in Fig. 7a. The calculations reveal that the Mo–B and B–B interactions contributes the most as compared to Mo–*A*, Y–B, Y–*A* and *A*–*A*. Here it is also demonstrated that the bonding in $Mo_{4/3}Y_{2/3}AlB_2$ and $Mo_{4/3}Y_{2/3}GaB_2$ contribute similarly for all

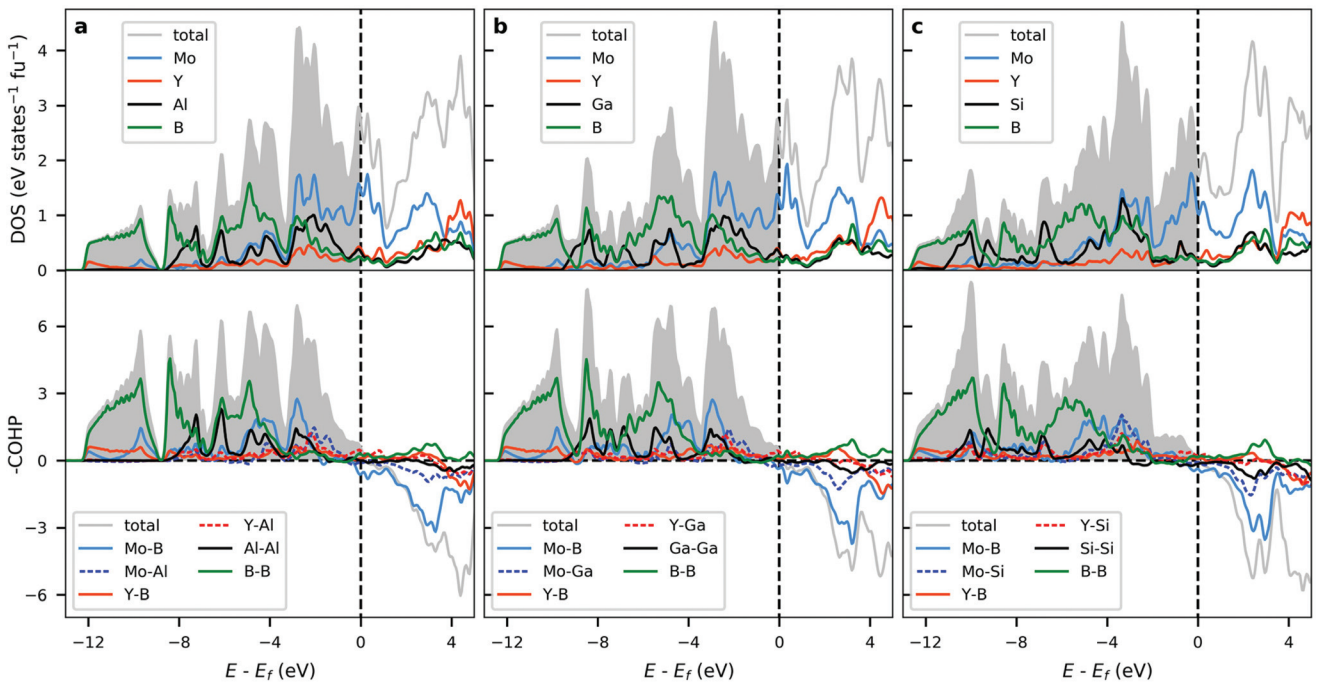

Fig. 6 Calculated total and atomic density of states (DOS) and total and projected crystal overlap Hamilton population (COHP) analysis for (a) $Mo_{4/3}Y_{2/3}AlB_2$, (b) $Mo_{4/3}Y_{2/3}GaB_2$, and (c) $Mo_{4/3}Y_{2/3}SiB_2$ of space group $R\bar{3}m$.

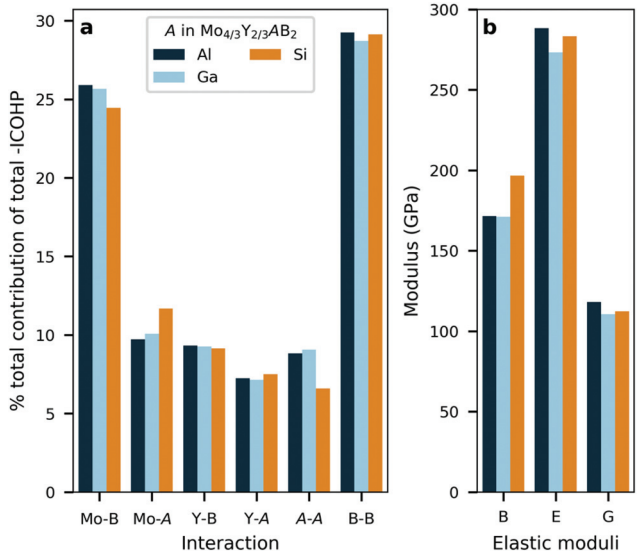

Fig. 7 (a) The contributions, in percentage, of selected interactions with respect to the net bonding for selected and (b) calculated elastic moduli – bulk modulus *B*, Young modulus *E* and Shear modulus *G*. Data shown for $Mo_{4/3}Y_{2/3}AB_2$ of space group $R\bar{3}m$ and *A* = Al, Ga, Si.

interactions. This in comparison with $Mo_{4/3}Y_{2/3}SiB_2$ where a slight increase for Mo–Si and a decrease for Si–Si is observed. Note that the multiplicity for each type of interaction is included in the net contribution. Individual bond strengths and comparison between different interactions may differ, but these do not change the identified overall trends in bonding.

The similar bonding characteristics among the three stable $Mo_{4/3}Y_{2/3}AB_2$ *i*-MAB phases – with *A* = Al, Ga, Si – is also reflected in Fig. 7b, where bulk modulus *B*, Young modulus *E*, and Shear modulus *G* is shown. When comparing Al, Ga and Si, we find only minor differences, although the bulk modulus is slightly larger for *A* = Si. Fig. S58 and Table S8† further shows that these results are independent of the assigned symmetry. A more detailed analysis of impact from different metals in $M'_{4/3}M''_{2/3}AlB_2$ on mechanical properties can be found in ref. 65.

Conclusion

In summary, through a systematic theoretical study of the phase stability of quaternary $(M'_{1-x}M''_x)_2AB_2$ (212) MAB phases upon alloying between *M′* and *M″* from group 3 to 9 (Sc, Y, Ti, Zr, Hf, V, Nb, Ta, Cr, Mo, W, Mn, Fe, Co) combined with various *A*-elements (Al, Ga, In, Si, Ge, Sn), we confirm all experimentally synthesized phases to date with both chemical order (*i*-MAB) and solid solution disorder. Importantly, beyond *A* = Al we also predict an additional 21 thermodynamically and dynamically stable *i*-MAB phases and 36 stable solid solutions (1 with *Cmmm* symmetry and 35 with $P\bar{6}m2$ symmetry). These hypothetical phases remain to be experimentally verified, and synthesis is encouraged. Preference for order or solid solution upon metal alloying in 212 MAB phases are dictated mainly by the size difference between the alloying metal elements. Ordered *i*-MAB phases are energetically favoured when *M″* is larger than *M′* by at least 0.2 Å. This is typically fulfilled for *M′* = Cr, Mo, Mn, or Fe combined with *M″* = Sc or Y, and with *A* = Al, Ga, and Si. Phases with similar size of *M′* and *M″* show preference for solid solution, with *Cmmm* being favoured for *A* = Al while $P\bar{6}m2$ being favored for *A* = Ga, in, Ge, and Sn. Further investigation of selected *i*-MAB phases promising for synthesize reveals that different *A*-elements only have minor impact on the bonding characteristics and hence similar properties are expected. This study demonstrates that alloying is viable path towards novel elemental combinations to extend the frontier of MAB phase chemistries which, in turn, allows for potentially tuneable and advantageous properties.

Author contributions

The manuscript was written through contributions from all authors.

Conflicts of interest

There are no conflicts to declare.

Acknowledgements

We acknowledge support from the Knut and Alice Wallenberg (KAW) Foundation for a Fellowship/Scholar Grant and Project funding (KAW 2020.0033). Support from the Swedish Government Strategic Research Area in Materials Science on Functional Materials at Linköping University (Faculty Grant SFO-Mat-LiU No 2009 00971) is also acknowledged. The calculations were carried out using supercomputer resources provided by the Swedish National Infrastructure for Computing (SNIC) at the National Supercomputer Centre (NSC), the High Performance Computing Center North (HPC2N), and the PDC Center for High Performance Computing partially funded by the Swedish Research Council through grant agreement no. 2018-05973.

References

1 H. J. Becher, K. Krogmann and E. Peisker, *Z. Anorg. Allg. Chem.*, 1966, **344**, 140–147.
2 W. Jeitschko, *Acta Crystallogr., Sect. B: Struct. Crystallogr. Cryst. Chem.*, 1969, **25**, 163.
3 N. F. Chaban and I. U. B. KuzMa, *Izv. Akad. Nauk SSSR, Neorg. Mater.*, 1973, **9**, 1908–1911.
4 X. Tan, P. Chai, C. M. Thompson and M. Shatruk, *J. Am. Chem. Soc.*, 2013, **135**, 9553–9557.
5 M. Ade and H. Hillebrecht, *Inorg. Chem.*, 2015, **54**, 6122–6135.

6 L. Verger, S. Kota, H. Roussel, T. Ouisse and M. W. Barsoum, *J. Appl. Phys.*, 2018, **124**, 205108.
7 Y. Zhou, H. Xiang, F.-Z. Dai and Z. Feng, *Mater. Res. Lett.*, 2017, **5**, 440–448.
8 S. Kota, W. Wang, J. Lu, V. Natu, C. Opagiste, G. Ying, L. Hultman, S. J. May and M. W. Barsoum, *J. Alloys Compd.*, 2018, **767**, 474–482.
9 W. Rieger, H. Nowotny and F. Benesovsky, *Monatsh. Chem.*, 1965, **96**, 844–851.
10 W. Jeitschko, *Monatsh. Chem.*, 1966, **97**, 1472–1476.
11 Y. Zhang, S. Okada, T. Atoda, T. Yamabe and I. Yasumori, *J. Ceram. Assoc. Jpn.*, 1987, **95**, 374–380.
12 H. Zhang, F.-Z. Dai, H. Xiang, Z. Zhang and Y. Zhou, *J. Mater. Sci. Technol.*, 2018, **35**, 530–534.
13 S. Kota, E. Zapata-Solvas, A. Ly, J. Lu, O. Elkassabany, A. Huon, W. E. Lee, L. Hultman, S. J. May and M. W. Barsoum, *Sci. Rep.*, 2016, **6**, 26475.
14 L. T. Alameda, C. F. Holder, J. L. Fenton and R. E. Schaak, *Chem. Mater.*, 2017, **29**, 8953–8957.
15 D. K. Mann, J. Xu, N. E. Mordvinova, V. Yannello, Y. Ziouani, N. González-Ballesteros, J. P. S. Sousa, O. I. Lebedev, Y. V. Kolen'ko and M. Shatruk, *Chem. Sci.*, 2019, **10**, 2796–2804.
16 L. T. Alameda, P. Moradifar, Z. P. Metzger, N. Alem and R. E. Schaak, *J. Am. Chem. Soc.*, 2018, **140**, 8833–8840.
17 H. Zhang, F.-Z. Dai, H. Xiang, X. Wang, Z. Zhang and Y. Zhou, *J. Mater. Sci. Technol.*, 2019, **35**, 1593–1600.
18 M. Khazaei, J. Wang, M. Estili, A. Ranjbar, S. Suehara, M. Arai, K. Esfarjani and S. Yunoki, *Nanoscale*, 2019, **11**, 11305–11314.
19 L. T. Alameda, R. W. Lord, J. A. Barr, P. Moradifar, Z. P. Metzger, B. C. Steimle, C. F. Holder, N. Alem, S. B. Sinnott and R. E. Schaak, *J. Am. Chem. Soc.*, 2019, **141**, 10852–10861.
20 K. Kim, C. Chen, D. Nishio-Hamane, M. Okubo and A. Yamada, *Chem. Commun.*, 2019, **55**, 9295–9298.
21 J. Wang, T.-N. Ye, Y. Gong, J. Wu, N. Miao, T. Tada and H. Hosono, *Nat. Commun.*, 2019, **10**, 2284.
22 N. Miao, J. Wang, Y. Gong, J. Wu, H. Niu, S. Wang, K. Li, A. R. Oganov, T. Tada and H. Hosono, *Chem. Mater.*, 2020, **32**, 6947–6957.
23 Y. Yu and T. Lundström, *J. Alloys Compd.*, 1995, **226**, 5–9.
24 S. Okada, K. Iizumi, K. Kudaka, K. Kudou, M. Miyamoto, Y. Yu and T. Lundström, *J. Solid State Chem.*, 1997, **133**, 36–43.
25 L. A. Hanner, H. O. Badr, M. Dahlqvist, S. Kota, J. Rosen and M. W. Barsoum, *Mater. Res. Lett.*, 2021, **9**, 112–118.
26 P. Chai, S. A. Stoian, X. Tan, P. A. Dube and M. Shatruk, *J. Solid State Chem.*, 2015, **224**, 52–61.
27 Q. Du, G. Chen, W. Yang, J. Wei, M. Hua, H. Du, C. Wang, S. Liu, J. Han, Y. Zhang and J. Yang, *J. Phys. D: Appl. Phys.*, 2015, **48**, 335001.
28 S. Hirt, F. Yuan, Y. Mozharivskyj and H. Hillebrecht, *Inorg. Chem.*, 2016, **55**, 9677–9684.
29 F.-Z. Dai, H. Xiang, Y. Sun and Y. Zhou, *J. Mater. Sci. Technol.*, 2019, **35**, 1432–1438.
30 P. Ma, S. Li, J. Hu, X. Lu, W. Yu and Y. Zhou, *J. Alloys Compd.*, 2020, **814**, 152290.
31 M. Naguib, G. W. Bentzel, J. Shah, J. Halim, E. N. Caspi, J. Lu, L. Hultman and M. W. Barsoum, *Mater. Res. Lett.*, 2014, **2**, 233–240.
32 M. Dahlqvist, A. Petruhins, J. Lu, L. Hultman and J. Rosen, *ACS Nano*, 2018, **12**, 7761–7770.
33 B. Anasori, M. Dahlqvist, J. Halim, E. J. Moon, J. Lu, B. C. Hosler, E. N. Caspi, S. J. May, L. Hultman, P. Eklund, J. Rosén and M. W. Barsoum, *J. Appl. Phys.*, 2015, **118**, 094304.
34 M. Dahlqvist, Q. Tao, J. Zhou, J. Palisaitis, P. O. Å. Persson and J. Rosen, *J. Am. Chem. Soc.*, 2020, **142**, 18583–18591.
35 Q. Tao, M. Dahlqvist, J. Lu, S. Kota, R. Meshkian, J. Halim, J. Palisaitis, L. Hultman, M. W. Barsoum, P. O. Å. Persson and J. Rosen, *Nat. Commun.*, 2017, **8**, 14949.
36 B. Ahmed, A. E. Ghazaly and J. Rosen, *Adv. Funct. Mater.*, 2020, **30**, 2000894.
37 A. Mockute, Q. Tao, M. Dahlqvist, J. Lu, S. Calder, E. N. Caspi, L. Hultman and J. Rosen, *Phys. Rev. Mater.*, 2019, **3**, 113607.
38 G. Kresse and J. Hafner, *Phys. Rev. B: Condens. Matter Mater. Phys.*, 1993, **47**, 558–561.
39 G. Kresse and J. Furthmüller, *Comput. Mater. Sci.*, 1996, **6**, 15–50.
40 G. Kresse and J. Furthmüller, *Phys. Rev. B: Condens. Matter Mater. Phys.*, 1996, **54**, 11169–11186.
41 P. E. Blöchl, *Phys. Rev. B: Condens. Matter Mater. Phys.*, 1994, **50**, 17953–17979.
42 G. Kresse and D. Joubert, *Phys. Rev. B: Condens. Matter Mater. Phys.*, 1999, **59**, 1758–1775.
43 J. P. Perdew, K. Burke and M. Ernzerhof, *Phys. Rev. Lett.*, 1996, **77**, 3865–3868.
44 H. J. Monkhorst and J. D. Pack, *Phys. Rev. B: Solid State*, 1976, **13**, 5188–5192.
45 R. Dronskowski and P. E. Bloechl, *J. Phys. Chem.*, 1993, **97**, 8617–8624.
46 V. L. Deringer, A. L. Tchougréeff and R. Dronskowski, *J. Phys. Chem. A*, 2011, **115**, 5461–5466.
47 S. Maintz, V. L. Deringer, A. L. Tchougréeff and R. Dronskowski, *J. Comput. Chem.*, 2013, **34**, 2557–2567.
48 R. Nelson, C. Ertural, J. George, V. L. Deringer, G. Hautier and R. Dronskowski, *J. Comput. Chem.*, 2020, **41**, 1931–1940.
49 A. Zunger, S. H. Wei, L. G. Ferreira and J. E. Bernard, *Phys. Rev. Lett.*, 1990, **65**, 353–356.
50 M. Dahlqvist, B. Alling, I. A. Abrikosov and J. Rosén, *Phys. Rev. B: Condens. Matter Mater. Phys.*, 2010, **81**, 024111.
51 M. Dahlqvist, B. Alling and J. Rosén, *Phys. Rev. B: Condens. Matter Mater. Phys.*, 2010, **81**, 220102.
52 P. Eklund, M. Dahlqvist, O. Tengstrand, L. Hultman, J. Lu, N. Nedfors, U. Jansson and J. Rosén, *Phys. Rev. Lett.*, 2012, **109**, 035502.
53 A. S. Ingason, A. Mockute, M. Dahlqvist, F. Magnus, S. Olafsson, U. B. Arnalds, B. Alling, I. A. Abrikosov,

B. Hjörvarsson, P. O. Å. Persson and J. Rosen, *Phys. Rev. Lett.*, 2013, **110**, 195502.
54 A. S. Ingason, A. Petruhins, M. Dahlqvist, F. Magnus, A. Mockute, B. Alling, L. Hultman, I. A. Abrikosov, P. O. Å. Persson and J. Rosen, *Mater. Res. Lett.*, 2014, **2**, 89–93.
55 A. Mockute, M. Dahlqvist, J. Emmerlich, L. Hultman, J. M. Schneider, P. O. Å. Persson and J. Rosen, *Phys. Rev. B: Condens. Matter Mater. Phys.*, 2013, **87**, 094113.
56 A. Mockute, P. O. Å. Persson, F. Magnus, A. S. Ingason, S. Olafsson, L. Hultman and J. Rosen, *Phys. Status Solidi RRL*, 2014, **8**, 420–423.
57 A. Thore, M. Dahlqvist, B. Alling and J. Rosén, *Comput. Mater. Sci.*, 2014, **91**, 251–257.
58 K. Momma and F. Izumi, *J. Appl. Crystallogr.*, 2011, **44**, 1272–1276.
59 D. Potashnikov, E. N. Caspi, A. Pesach, S. Kota, M. Sokol, L. A. Hanner, M. W. Barsoum, H. A. Evans, A. Eyal, A. Keren and O. Rivin, *Phys. Rev. Mater.*, 2020, **4**, 084404.
60 D. Potashnikov, E. N. Caspi, A. Pesach, A. Hoser, S. Kota, L. Verger, M. W. Barsoum, I. Felner, A. Keren and O. Rivin, *J. Magn. Magn. Mater.*, 2019, **471**, 468–474.
61 L. Ke, B. N. Harmon and M. J. Kramer, *Phys. Rev. B*, 2017, **95**, 104427.
62 W. Hume-Rothery, R. E. Smallman and C. W. Haworth, *The structure of metals and alloys*, The Institute of Metals, London, 1969.
63 M. Dahlqvist and J. Rosen, *Nanoscale*, 2020, **12**, 785–794.
64 M. Dahlqvist, J. Lu, R. Meshkian, Q. Tao, L. Hultman and J. Rosen, *Sci. Adv.*, 2017, **3**, e1700642.
65 H. Lind, M. Dahlqvist and J. Rosen, *J. Phys.: Condens. Matter*, 2021, **33**, 255402.